

Suzuki segregation behavior and mechanism in a Co–Cr–Fe–Ni–Mo high-entropy alloy

Jiaxiang Li^a, Kenta Yamanaka^{b,*}, Junhua Hu^a, Akihiko Chiba^b

^a School of Materials Science and Engineering, Zhengzhou University, Zhengzhou, 450001, China

^b Institute for Materials Research, Tohoku University, 2-1-1 Katahira, Aoba-ku, Sendai, 980-8577, Japan



ARTICLE INFO

Keywords:

High-entropy alloy
Interface segregation
Density functional theory
MC simulation
Stacking fault energy

ABSTRACT

The knowledge of the Suzuki effect in compositionally complex CoNiCrMo and CoCrFeNiMo solid-solution alloys is rather limited. In this study, the enrichment of Co and Mo atoms and depletion of Cr, Fe, and Ni atoms were determined within the region of four atomic layers at stacking faults (SFs) in a typical quinary concentrated solid-solution alloy ($\text{Co}_{0.95}\text{Cr}_{0.8}\text{Fe}_{0.25}\text{Ni}_{1.8}\text{Mo}_{0.475}$) by using scanning transmission electron microscopy and energy dispersive X-ray spectroscopy. To better understand the Suzuki effect, two-stage first-principles Monte Carlo (MC) simulations each with up to 3000 trial swap steps were performed. First, the simulation results suggested the strong tendency of Mo segregation at the second nearest neighbor (2NN) sites at SFs. Nonetheless, as a further Mo segregation induces the excessively large lattice distortion and intrinsic strain energy, it would be inhibited. It was deemed one potential reason for the finite Mo segregation. Second, the simulations revealed the origin and formation of co-segregation of Co and Mo atoms. The segregated Mo atoms at the 2NN sites attract Co atoms, forming the local $\text{D}0_{19}$ -type ordering at SFs. As a consequence, the stacking fault energy can reach a strongly negative value below -500 mJ/m^2 . Meanwhile, the Co/Mo co-segregated SFs have high stability against phase transitions to intermetallics and martensite at 773 K.

1. Introduction

Interactions between defects and alloy atoms are common in structural materials. A stacking fault (SF) in FCC alloys is generated when the local HCP structure with ABAB-type stacking sequence is embedded in the FCC matrix. From the viewpoint of energetics, some atoms would prefer the HCP structure to the FCC matrix, and thus segregate at the SFs. The kind of chemical interaction between SFs and some atoms refers to the Suzuki effect, which causes Suzuki segregation and age hardening of alloys after cold working [1–4]. Particularly in high-entropy alloys (HEAs) with complex composition [5,6], there presumably exist specific constituent atoms more stable in the HCP structure. While there is no direct evidence for age hardening via the Suzuki effect in CoCrFeNiMn HEA [7] and CoCrNi medium-entropy alloy [8], the age hardening is remarkable in CoNiCrMo alloy [3] and CoCrFeNiMo HEA [4]. Mo is a strongly segregating element to the SFs [3,4,9,10].

For understanding of the Suzuki effect and the development of strong materials, Suzuki segregation needs to be quantitatively measured. Over the past few decades, the Suzuki hardening is reported in compositionally complex FCC solid-solution alloys, but it is a technical challenge

to completely determine Suzuki segregation, owing to the small variations of elemental concentrations at SFs compared to those at dislocations and grain boundaries [11]. Koizumi et al. [9] simulated Suzuki segregation in CoNiCrMoNb superalloys using a thermodynamics-based phase-field model and remarked that the model should be improved by considering the atomic size difference and intrinsic strain effect on the segregation behavior. However, it is beyond the bounds of thermodynamic evaluation to separate the intrinsic strain energy from the Gibbs energy derived with thermodynamic parameters. In theory, the segregation energy could be described as a sum of three parts: the changes in chemical energy, in intrinsic strain energy, and in gradient energy. In most cases, the intrinsic strain energy is considered small, the change of which is neglected in the thermodynamic calculations of stacking fault energy (SFE) [12,13]. Although it is generally accepted that the chemical attraction between some specific atoms and SFs plays a dominant role in Suzuki segregation, the variation in local lattice distortion and intrinsic strain energy at SFs should also be taken into account, particularly in alloys where the differences in atomic sizes are large. In the CoNiCrMo alloys [3,9,14–16], CoCrFeNiMo HEA [4], and many other similar alloys (1 at% < Mo concentration ≤ 6.5 at%), Mo has a relatively

* Corresponding author.

E-mail address: kenta.yamanaka.c5@tohoku.ac.jp (K. Yamanaka).

large atomic size. While Mo is a key element that induces the Suzuki hardening in these alloys, the segregation behavior and mechanism of Mo atoms are yet unclear. Electronic-scale density functional theory (DFT) calculation is a powerful tool in estimating the interface structure, chemistry, and properties [17,18]. With the advancements in supercomputing, DFT-based Monte Carlo (MC) simulations using atomistic discrete models can provide reliable information on the real-time evolution of atomic arrangement over large time scales. Thus, the DFT-based MC method becomes a viable option for simulating Suzuki segregation and monitoring local intrinsic strain.

In this study, two-stage DFT-based MC simulations of Suzuki segregation were performed to clarify firstly the intricate segregation behavior of Mo atoms and then the origin and formation of Co/Mo co-segregation in a 11.11 at% Mo-containing CoCrFeNi-based HEA [19]. Based on the simulation results, we proposed a new mechanism for finite Suzuki segregation of Mo, elucidated the role of each constituent element in the Suzuki effect, and finally discussed the stability of Co/Mo co-segregated SFs. This work moves forward in understanding the Suzuki effect in complex concentrated solid-solution alloys and enriches the knowledge base of designing materials via interface engineering.

$$\gamma(T) = (F_{SF}(T) - F_{Perf.}(T)) / A = (\Delta E_{SF-Perf.} + P\Delta V + \Delta F_{phon.}(T) + \Delta F_{ele.}(T) + \Delta F_{conf.}(T) + \Delta F_{mag.}(T)) / A. \quad (2)$$

2. Methods

2.1. Materials and experiments

A solution-treated specimen of $\text{Co}_{0.95}\text{Cr}_{0.8}\text{Fe}_{0.25}\text{Ni}_{1.8}\text{Mo}_{0.475}$ HEA was tensile strained to 10% and was aged at 773 K for 72 h. The tensile-aged microstructure was characterized using scanning electron microscopy (SEM, S-3400N, Hitachi), electron backscattered diffraction (EBSD, OIM, EDAX) and X-ray diffraction (XRD, X'pert MPD, PANalytical). A specimen for scanning transmission electron microscopy (STEM) observations was prepared using a focused ion beam-scanning electron microscopy (FIB-SEM) FEI Helios NanoLab 600i dual-beam system. A double spherical aberration-corrected STEM (Titan³ G2 60-300, FEI) equipped with a Super-X energy dispersive X-ray spectroscopy (EDS) system was used to perform local chemical analysis around SFs.

2.2. First-principles MC simulations and DFT calculations

The Vienna *Ab initio* Simulation Package (VASP) [20] was used for DFT calculations and DFT-based MC simulations. In the relaxation and static calculations of supercells, the plane-wave cutoff energy was set to 350 eV. An energy change smaller than 1×10^{-5} eV and a Hellmann–Feynman force less than 1×10^{-3} eV/Å were adopted as the condition for convergence. A Monkhorst–Pack k -point mesh of $9 \times 9 \times 1$ was used for the calculations of 0-K enthalpy and phonon free energy, and a sparser mesh of $6 \times 6 \times 1$ was used in the MC simulations. Spin polarization (ISPIN = 2) was enabled in the calculations at 0 K.

An initial SF-containing, monoclinic supercell consisting of 48 atoms on twelve FCC (111) planes and a vacuum layer of 10 Å (#0 supercell in Fig. 2c–l) was constructed. Zhao et al. [21] have suggested that nine (111) planes are sufficient to obtain accurate SFEs for pure Ni. For the simulation of HEA composition, the larger supercell with more (111) planes was adopted here. The elements were distributed so evenly that the numbers of atoms with the same element type were the same or different by one atom on the two sides of SF and every (111) plane did not contain two or more atoms with the same element type involving Co, Cr, Fe, and Mo. If necessary, each first-principles MC simulation can be

run for 3000 trial swap steps, according to the following rules of sampling, swap, and acceptance. In each trial step, two random nearest neighbor (NN) atoms of different elements on the same side of SF were swapped. The relaxation of internal ionic positions of supercell equal to five ionic steps was performed, and the instantaneous energy of the supercell at the fifth ionic step (E) along with the internal ionic positions were noted. If the energy of the supercell decreased after the swap, the swap was successful; if the variation in energy at a trial swap step (∂E) was positive, the swap was considered successful with the probability

$$p = \exp(-\partial E / (kT)), \quad (1)$$

where k is the Boltzmann constant and T is the applied temperature (773 K). The next trial swap was initiated from the supercell of the last successful swap. Limitations of MC simulations herein are the five limited ionic steps and devoid of the temperature effect. The effectiveness of first-principles MC simulations has been validated in Appendix A.

For the supercells obtained from the MC simulations, the SFE (γ) was independently calculated with the fault plane shift between two adjacent (111) planes [22]. The method is appropriate for the investigation of the effect of local chemical environment and elemental segregation on fault energy. The SFE at finite temperatures is expressed as below:

In Eq. (2), $F_{SF}(T)$ and $F_{Perf.}(T)$ are the Helmholtz free energy of the faulted and perfect FCC supercells, respectively. The perfect FCC supercell is generated by removing the SF from the faulted counterpart. A is the SF area of the faulted FCC supercell. $\Delta E_{SF-Perf.}$ is the difference between the faulted and perfect FCC supercells in DFT-calculated ground-state energy. ΔV is the volume change with the interface removement from a faulted FCC supercell, which is negligible. The term $P\Delta V$ can be omitted. $\Delta F_{phon.}(T)$, $\Delta F_{ele.}(T)$, $\Delta F_{conf.}(T)$, and $\Delta F_{mag.}(T)$ are the differences in phonon, thermal electronic, configurational, and magnetic free energy, respectively; the four terms change with temperature. A general method with the quasi-harmonic approximation was employed to calculate the free energies at the finite temperatures, as implemented in the code PHONOPY [23]. Supercell and finite displacement approaches were used to obtain the atomic forces and calculate the phonon free energy. The details were described in Appendix B. Faulted and perfect FCC supercells have the same atomic configuration except for the fault plane. As the first-order approximation, the differences in phonon and thermal electronic free energies of the four-layer atoms around the SF plane between faulted and perfect FCC supercells were calculated. The results for different supercells are shown in Figs. S1–S3. Moreover, the configurational free energy is related to the configurational entropy; that is, $\Delta F_{conf.}(T) = -T \bullet \Delta S_{conf.}(T)$. The configurational entropy is approximated by the ideal entropy of mixing; $\Delta S_{conf.}(T) = -k \sum c_i \ln c_i$, where c_i is the mole fraction of element i . Since perfect and faulted FCC supercells have the same atomic concentrations, $\Delta S_{conf.}(T)$ is equal to zero. Thus, $\Delta F_{conf.}(T)$ is ignored in the calculation of SFE. Using the CALPHAD method [13] and a commercially provided thermodynamic database (TCHEA5, Thermotech Ltd.), the Curie temperature of alloy is calculated as 236 K. At the temperature above 236 K, $F_{mag.}(T)$ of faulted and perfect FCC supercells can be both treated as zero.

3. Results

3.1. Determination of suzuki segregation

The HAADF-STEM image in Fig. 1a shows an edge-on SF vertically positioned in the middle. The EDS elemental distribution map in Fig. 1b

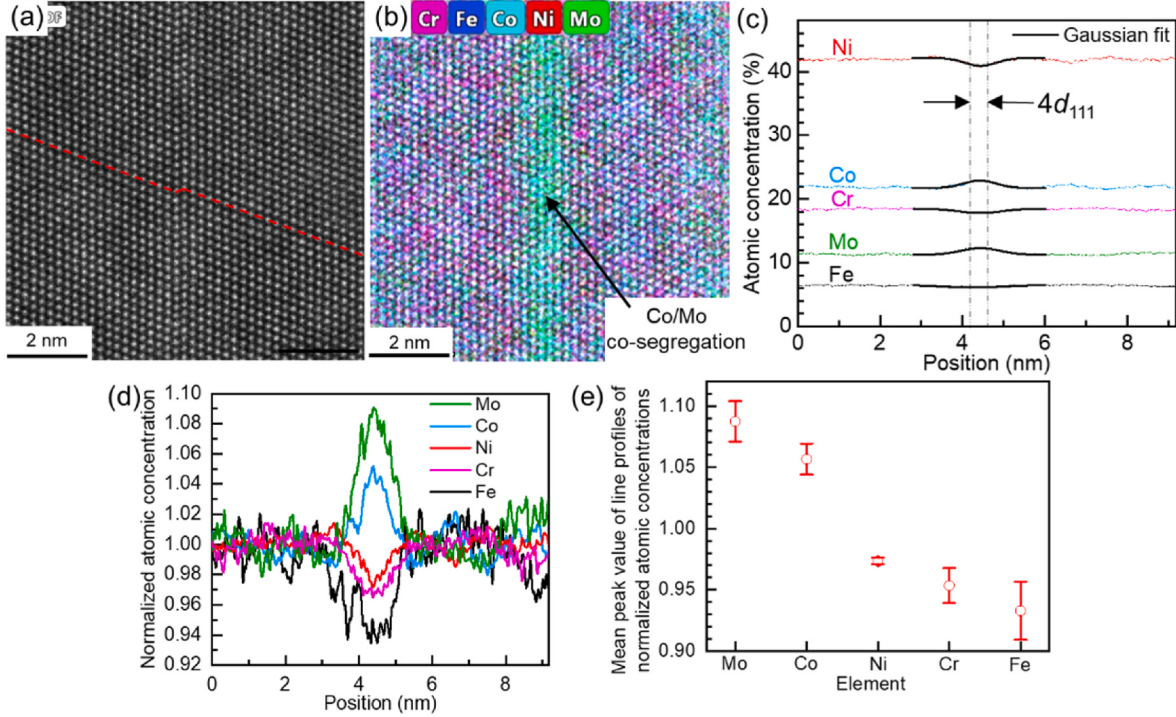


Fig. 1. (a) HAADF-STEM image with an edge-on SF vertically positioned in the middle, and (b) the EDS elemental distribution map. (c) Line profiles obtained by vertically integrating the horizontal EDS line scans in (b). (d) The line profiles after the normalization of atomic concentrations in (c). (e) The mean peak value of line profiles of normalized atomic concentrations based on four sets of measures.

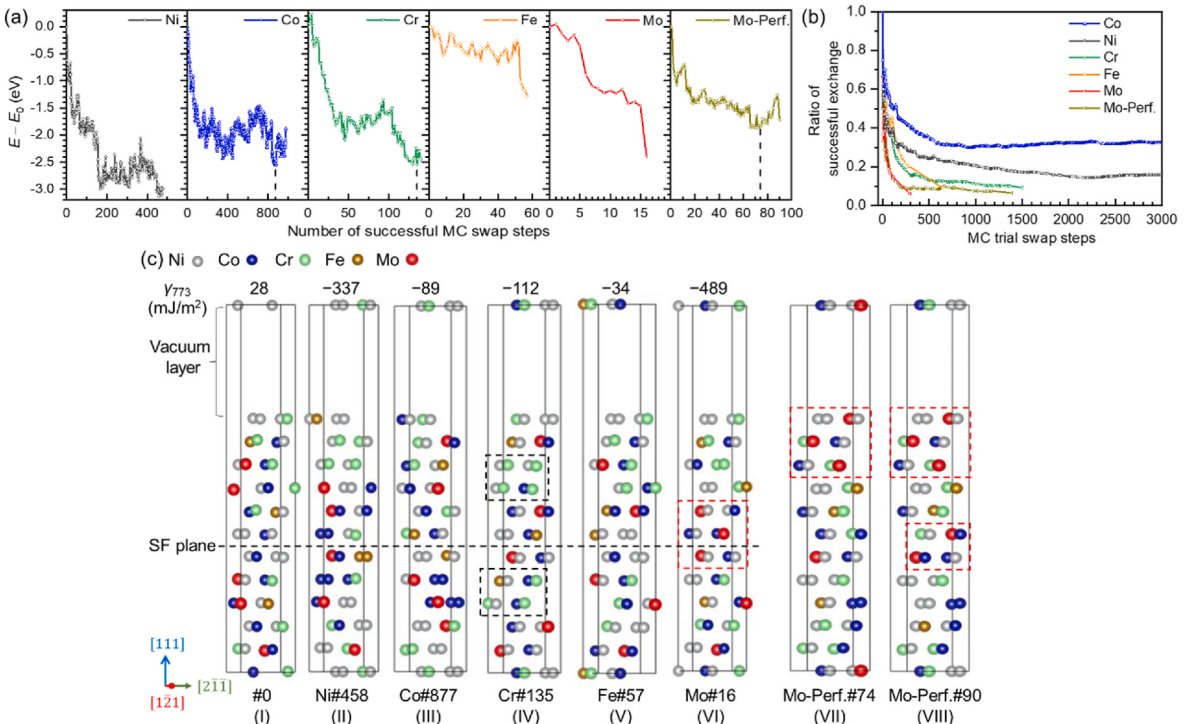


Fig. 2. (a) Energy variation of faulted FCC supercells with respect to the initial supercell, ($E - E_0$), subject to the condition of a successful MC swap in the MC simulations for different elements. (b) Ratios of successful MC swaps in the MC simulations for different elements. (c-I) The initial faulted FCC supercell (#0). The faulted FCC supercell that has the lowest energy during the entire MC simulation for (c-II) Ni, (c-III) Co, (c-IV) Cr, (c-V) Fe or (c-VI) Mo atoms. The SFE at 773 K (γ_{773}) is indicated on top of the supercells. (c-VII) Mo-Perf.#74 and (c-VIII) Mo-Perf.#90 supercells generated from a MC simulation for Mo atoms in perfect FCC supercells. The energy variation of perfect FCC supercells is shown on the right side of (a).

indicated that the SF was accompanied with co-segregation of Co and Mo atoms. The line profiles in Fig. 1c were obtained by vertically integrating the horizontal EDS line scans in the elemental distribution map. Due to the delocalization of the EDS signal [24], the variations of elemental concentrations at SFs exhibit a broad peak (trough). For the line profiles near the peak, Gaussian distribution fitting was conducted and superimposed in Fig. 1c. Their variances were in the range of 0.853–0.881 nm, which were approximately equal to the thickness of four (111) planes ($4d_{111}$, 0.868 nm), measured in Fig. 1a. Therefore, the Co and Mo atoms were enriched within the region of four atomic layers around the SF (defined as SF region hereafter). In Fig. 1d, the line profiles after the normalization of atomic concentrations further suggested heavier enrichment of Mo than that of Co, and heavier depletion of Fe than those of Ni and Cr. In Fig. 1e, the mean peak values of line profiles of normalized atomic concentrations based on four sets of measures show the similar trends.

3.2. Simulation results of suzuki segregation

3.2.1. The first stage results

MC simulations should run at least 10^4 MC trial swap steps per atom to reach thermodynamic equilibrium. It is almost impossible for MC simulations based on *ab initio* energetics to meet this condition. To accelerate convergence, in the first stage, the first-principles MC simulations were independently run five times in faulted FCC supercells, each swapping one certain element type of atoms with their NN atoms. Fig. 2a shows the energy variations of faulted FCC supercells with respect to the initial supercell, ($E - E_0$), subject to the condition of a successful swap. Fig. 2b shows the ratios of successful swaps in the MC simulations for different elements. We define convergence as the condition such that no successful swap occurs in the next 100 trial steps of a state. With this definition, the MC simulation for Mo, Fe, and Cr atoms converges at the 293rd, 645th, and 1497th trial steps, respectively, while the MC simulation for Ni or Co atoms does not converge within the 3000 trial steps. The supercells generated from the MC simulation for Ni or Co atoms are thus not deemed stable. The convergence, in the case of Fe atoms is related to the low Fe concentration: only three Fe atoms exist in the 48-atom supercells; the convergence in the case of Cr atoms is related to the formation of a stable short-range cluster of Cr atoms, as outlined with black frames in Fig. 2c–IV. The fastest decline in energy and the fastest convergence both occur in the MC simulation for Mo atoms. Moreover, in the MC simulation for Mo atoms, the calculated SFE at 773 K (γ_{773}) falls from 28 mJ/m² for the initial supercell (Fig. 2c–I) to -489 mJ/m² for the converged supercell (i.e., Mo#16 supercell shown in Fig. 2c–VI). Although the γ_{773} of the lowest-energy supercell during the entire simulation for Ni, Co, Cr, and Fe atoms decreases to the range -34 to -337 mJ/m² (Fig. 2c–II–V), the γ_{773} of Mo#16 supercell is the least. Note that two Mo atoms and a Co atom segregate in the first nearest neighbor planes (1NNPs) of SF in the Mo#16 supercell. The rapid decline in the energy in the MC simulation for Mo atoms may originate from Suzuki segregation of Mo and Co atoms. In contrast, because Mo atoms get few swapping opportunities in the other simulations, Mo segregation does not appear. Further, it is noticed that the Mo#16 supercell has three 2NN Mo atoms in the red-framed region at SFs. Starting from the corresponding perfect FCC supercell of #0 faulted supercell where the SF is removed with the fault plane shift method, another MC simulation was run for Mo atoms to evaluate the effect of forming the 2NN Mo atoms on the energetic stabilization of MC simulation. The energy variation of perfect FCC supercells is shown on the right of Fig. 2a, where the energy does not fall to a level as low as that of faulted FCC supercells. It converges at the 1387th trial step (Fig. 2b), the convergence of which is much slower than that of faulted FCC supercells in the MC simulation. The lowest-energy supercell (i.e., Mo-Perf.#74 supercell in Fig. 2c–VII) has three 2NN Mo atoms in the top red-framed region. The converged supercell (Mo-Perf.#90 supercell in Fig. 2c–VIII) has the same three 2NN Mo atoms. Although the Mo-Perf.

#90 supercell has another pair of the 2NN Mo atoms in the middle red-framed region, its energy is higher than that of Mo-Perf.#74 supercell. The formation of the 2NN Mo atoms is thus not a sufficient condition for the strong energetic stabilization of MC simulation for Mo atoms in faulted FCC supercells. The interaction between three 2NN Mo atoms and SF should be a decisive factor.

At low and intermediate temperatures, the studied CoCrFeNi-based HEA is a supersaturated solid-solution with a large lattice distortion owing to the Mo addition [19]. The lattice expands at the specific sites of Mo atoms, and the migration of Mo atoms would induce a significant variation in local lattice distortion. The large mean bond length (\overline{BL}) generally implies a highly expanded lattice and large lattice distortion induced by Mo in the CoCrFeNi-based HEAs [19]. The \overline{BL} of each supercell in the MC simulation for Mo atoms (i.e., Mo#0–#16 supercells in Fig. 3a) was calculated, and the results are presented in Fig. 3b. The large variations in \overline{BL} often occur due to interplanar migration of Mo atoms, which are highlighted with cyan-filling regions under the curve of \overline{BL} . In addition, the increase in Mo concentration in a region consisting of two or three adjacent layers contributes to an increase in \overline{BL} . For example, the magnitude of \overline{BL} for Mo#1, Mo#14, and Mo#15 supercells is positively correlated with the local Mo concentration in the red-framed regions; when a Mo atom migrates into the red-framed region, the \overline{BL} increases; when a Mo atom migrates out of the red-framed region, the \overline{BL} decreases. In contrast to the Mo#1 supercell, the red-framed region for the Mo#14 and Mo#15 supercells includes the central part of SF region. Fig. 3c shows the \overline{BL} in the SF region (\overline{BL}_{SF}) for Mo#0–#16 supercells. The evident increase in \overline{BL}_{SF} occurs due to the segregation of Mo atoms from the third nearest neighbor plane (3NNP) into the second nearest neighbor plane (2NNP) (e.g., in Mo#7 and Mo#14 supercells) and from the 2NNP into the 1NNP (e.g., in Mo#2, Mo#13, and Mo#15 supercells), as highlighted with cyan-filling regions under the curve of \overline{BL}_{SF} . \overline{BL}_{SF} reaches the largest value in the Mo#15 supercell. The large lattice distortion in the SF region of Mo#14 and Mo#15 supercells may influence the magnitude of SFE.

In the upper part of Fig. 4a, the γ_{773} and the SFE calculated with atomic relaxation at 0 K (named as the relaxed SFE (γ_R)) are presented for the Mo#0–#16 supercells. The increase in temperature from 0 to 773 K causes small variations in SFEs. Subsequent analyses focus on the γ_R . The local chemistry in the region up to the 3NNPs of SF for the Mo#1–#3 and Mo#12–#16 supercells is presented in Fig. 4b to understand the correlation between Mo segregation and the variation in γ_R . In these supercells, the variations in γ_R are evident, as highlighted with cyan-filling regions under the curve of γ_R . From the Mo#1 to #3 supercells, the γ_R decreases from 43, to 61, to -197 mJ/m², when the Mo atom, indicated with a red arrow, in the 2NNP of SF migrates into the 1NNP and then adjusts itself to another lower-energy position in the same plane. From the Mo#12 to #13 supercells, the Mo atom, indicated with a red arrow, in the 2NNP of SF migrates into the 1NNP; the process is accompanied with a large decrease in γ_R by 416 mJ/m². When two Mo atoms segregate at the 2NN sites in the two 1NNPs of SF, the γ_R of Mo#13 supercell reaches a low value. However, when the Mo atom, indicated with a blue arrow, migrates from the 3NNP inward into the 2NNP and then into the 1NNP, the reverse increase in γ_R is seen from the Mo#13 to #15 supercells.

To analyze the origin of the anomalous increase in γ_R associated with Mo segregation, the SFE calculated without atomic relaxation at 0 K (named as the unrelaxed SFE (γ_U)) and the difference between γ_R and γ_U ($\Delta\gamma = \gamma_R - \gamma_U$) are shown in the lower part of Fig. 4a. γ_R is the combined result of chemical interaction (γ_U) and structural relaxation ($\Delta\gamma$). For the Mo#1–#12 supercells, γ_U and $\Delta\gamma$ are in the range of ± 350 mJ/m². Starting from the Mo#13 supercell, γ_U falls to lower values and the $\Delta\gamma$ rises to higher values. The chemical interactions between two 2NN Mo atoms and Co/Ni atoms in the 1NNPs determine the small γ_U . Nonetheless, the Mo#15 supercell that has three Mo atoms in the 1NNPs, has

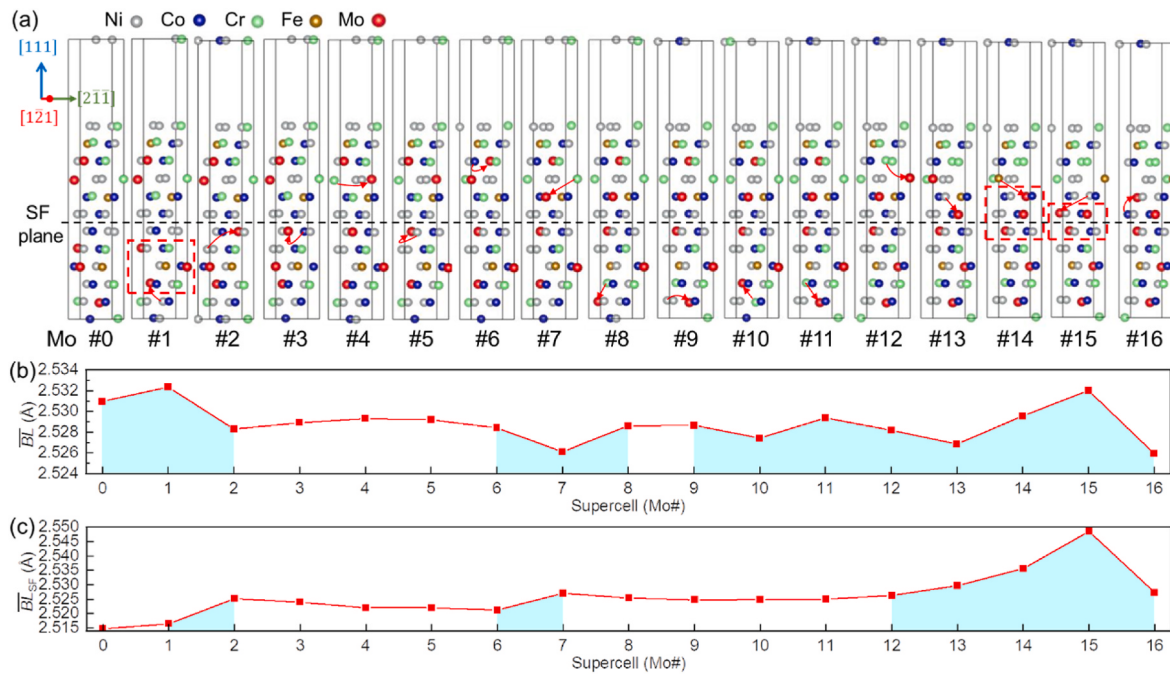


Fig. 3. (a) Evolution of atomic arrangement in the 1st stage simulation, Mo#0–#16 supercells, wherein the migration path of Mo atoms in the previous step is indicated with red arrows. (b) The magnitude of mean bond length (\overline{BL}) for each supercell. The interplanar migration steps of Mo atoms are highlighted with cyan-filling regions under the curve. (c) The magnitude of \overline{BL} in the SF region (\overline{BL}_{SF}) for each supercell. The interplanar migration steps with evident variations in \overline{BL}_{SF} , are highlighted with cyan-filling regions under the curve. (For interpretation of the references to colour in this figure legend, the reader is referred to the Web version of this article.)

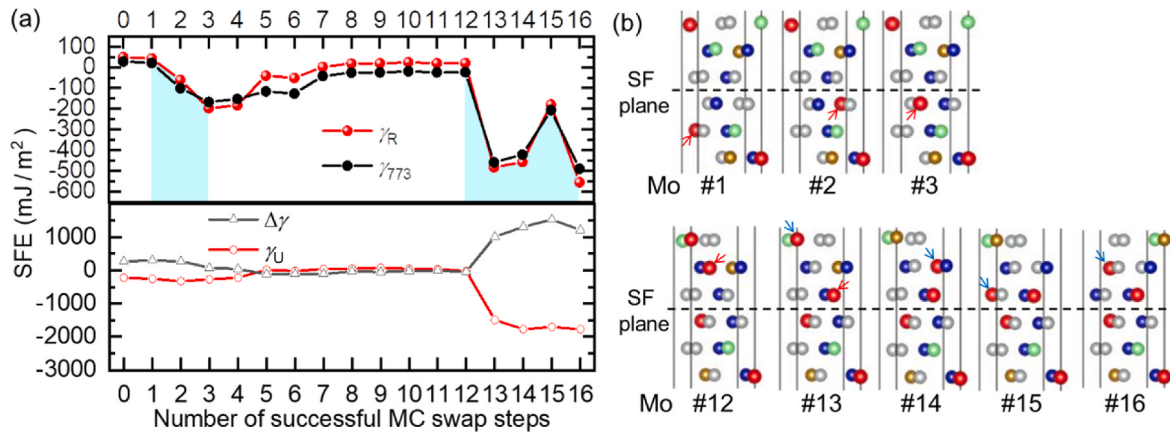


Fig. 4. (a) For the Mo#0–#16 supercells, the γ_{773} , the relaxed SFE (γ_R) at 0 K, unrelaxed SFE (γ_U) at 0 K, and the difference between γ_R and γ_U ($\Delta\gamma$). (b) Local chemistry in the region up to the third nearest neighbor planes of SF for the Mo#1–#3 and Mo#12–#16 supercells.

slightly larger γ_U than the Mo#14 and Mo#16 supercells. This implies that the higher Mo concentration in the 1NNPs of SF does not necessarily result in a smaller γ_U . Moreover, on the basis of the \overline{BL}_{SF} analysis above, it is inferred that the large lattice distortion in the SF region of Mo#14 and Mo#15 supercells contributes to the large intrinsic strain energy and $\Delta\gamma$. In fact, $\Delta\gamma$ increases from the Mo#13 to the Mo#15 supercell. The $\Delta\gamma$ of Mo#16 supercell is slightly lower than that of Mo#14 supercell, in contrast to the magnitudes of their \overline{BL}_{SF} . The increase in SFE after structural relaxation does not solely depend on the magnitude of intrinsic strain in the SF region. The intrinsic strain energy (φ) is described as a function of six independent elastic strain components ($\varepsilon_1, \varepsilon_2, \dots, \varepsilon_6$), as below [25]:

$$\varphi = V_0 / \left(2 \sum_{i=1}^6 \sum_{j=1}^6 C_{ij} \varepsilon_i \varepsilon_j \right), \quad (3)$$

where V_0 is the supercell volume without strain, and C_{ij} are independent elastic constants. Eq. (3) has two implications. The first implication is that the Mo atom with a larger atomic volume tends to induce the larger intrinsic strain energy; the second implication is that the magnitude of φ is related to C_{ij} . The C_{ij} for the SF region of Mo#13–#16 supercells and the calculation method are given in Appendix C1. To make a standardized comparison of C_{ij} , the elastic moduli were estimated based on the C_{ij} . As shown in Fig. C1, the elastic moduli for the Mo#16 supercell are obviously greater than those for other supercells. Although the \overline{BL}_{SF} of Mo#16 supercell is close to that of Mo#13 supercell, the larger elastic moduli lead to a significantly larger φ and $\Delta\gamma$ of Mo#16 supercell.

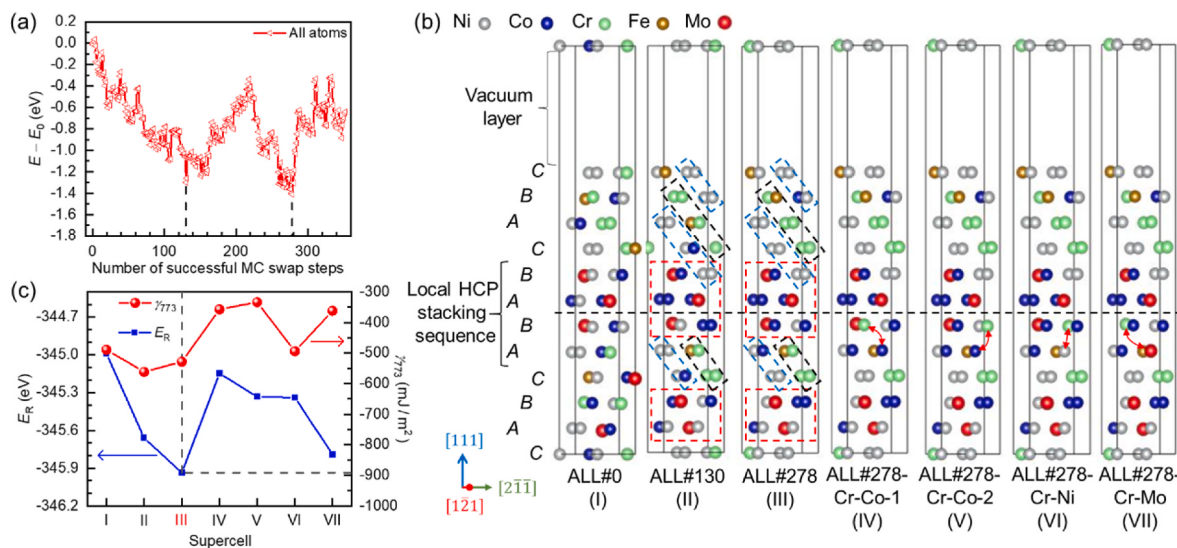


Fig. 5. (a) During the MC simulation without distinguishing between the element types, energy variation of faulted FCC supercells with respect to the initial Mo#16 supercell (labeled as ALL#0 supercell), ($E - E_0$), on condition of successful MC swaps. Two supercells, (b-II) ALL#130 and (b-III) ALL#278, corresponding to the lowest-energy state in two V-shaped variations. (b-IV, V, VI, VII) Altered ALL#278 supercells, wherein the atom indicated with a red double-headed arrow has been swapped. (c) Energy after full relaxation (E_R) and γ_{773} for the I–VII supercells in (b). (For interpretation of the references to colour in this figure legend, the reader is referred to the Web version of this article.)

Once the Mo atom, indicated with a blue arrow, migrates back from the 1NNP to another site in the 2NNP, the three Mo atoms in the SF region of Mo#16 supercell are located at the 2NN sites in three adjacent (111) planes; γ_U decreases significantly as γ_U and $\Delta\gamma$ decrease. This indicates that the number of Mo atoms that can be accommodated in the 1NNPs of SF is finite and the segregated Mo atoms preferentially occupy the 2NN sites in adjacent planes.

3.2.2. The second stage results

To examine the stability of Mo#16 supercell obtained, in the second stage, the MC simulation was run without distinguishing between the element types for 3000 MC trial swap steps with the Mo#16 supercell as a starting point (labeled as ALL#0 supercell). Fig. 5a shows two V-shaped variations in the curve of ($E - E_0$) on condition of a successful swap. Two supercells, corresponding to the lowest-energy state of two V-shaped variations, i.e., ALL#130 and ALL#278, are shown in Fig. 5b-II and 5b-III. Comparing the ALL#130, ALL#278 supercells with ALL#0 supercell shown in Fig. 5b-I, the pre-existing Mo atoms in the SF region retain their positions and the local Mo concentration is unchanged; two Co atoms segregate into the 1NNPs and the local Co concentration increases at the cost of a decrease in the local Ni concentration. The SFEs decrease a little from ALL#0 to ALL#130 and ALL#278 supercells by 73 and 39 mJ/m², respectively (Fig. 5c). As outlined with red frames, the local chemistry and structure of ALL#130 and ALL#278 supercells are analogous to those of the HCP D0₁₉ ordered structure [26,27]. The eight-atom unit cell of D0₁₉ Co₃Mo ordered structure is such that the two 2NN Mo atoms are located in neighboring (111) planes and the six other sites are occupied by Co atoms. The D0₁₉-type ordering in the SF region consists of three-layer atoms in the HCP stacking sequence, suggesting that SFs provide the structural basis for co-segregation of Co and Mo atoms. Site occupancies of Co and Mo atoms in the local D0₁₉-type ordering could be interpreted in terms of strong tendency of the NN Co–Mo pairing [25] and the fact that the NN Mo–Mo pairing results in an increase in the local intrinsic strain and energy (e.g., Mo#14 and Mo#15 supercells). Not only within the finite-sized supercells, but in the as-duplicated supercells along the [211] and [121] directions, the Mo atoms in the SF region are at the 2NN sites. This confirms the real formation of D0₁₉-type ordering in the SF region and the suitability of the (111) planar dimensions of supercells. Outside the SFs, short-range

clusters composed of mainly Cr and fewer Fe atoms or mainly Ni and fewer Co atoms are formed on (100) planes, as outlined with black or blue frames. Ding et al. [28] acquired EDS elemental distribution maps in an FCC CoCrFeNi-based HEA, where Cr- or Ni-rich atomic columns form a short line and triangle on (100) and (111) planes; they also claimed that the definite chemistry of atomic columns should be further confirmed. The current simulation result suggests that the short-range clusters outside the SFs preferentially form on the (100) planes.

4. Discussion

4.1. Mechanism for finite suzuki segregation of Mo

In terms of the simulation results, the chemical interactions between the Mo atoms at the 2NN sites and Co/Ni atoms in the two 1NNPs are highly efficient in the decreasing γ_U . The segregation of the 3rd Mo atom in the 1NNPs does not reduce the γ_U anymore. Moreover, when the 3rd Mo atom is located at the NN sites to the pre-existing Mo atoms in the SF region, γ_R increases due to increased $\Delta\gamma$ and local lattice distortion. Further segregation of Mo atoms is thus inhibited. The finite Mo atoms are regularly distributed at the 2NN sites in the SF region, which strikes a balance between chemical effect and lattice distortion effect. This is beyond the general understanding of the mechanism for finite Suzuki segregation, namely, the weakening of chemical attraction of SFs to unsegregated atoms of the same element type after the preceding segregation.

4.2. Origin and formation of Co/Mo co-segregation

The calculated γ_{773} of FCC pure Co is -141 mJ/m^2 . In comparison, synergistic segregation of Co and Mo atoms at SFs results in an even lower γ_{773} , e.g., -528 mJ/m^2 of ALL#278 supercell. The first-principles MC simulations indicate that, among the constituent elements, Mo has the strongest tendency to segregate at SFs. Although Co itself has segregation tendency at SFs [29], the rapidly segregated Mo atoms attract the Co atoms to the SFs, promoting co-segregation phenomenon. The strong tendencies of the NN Co–Co, Co–Mo, Ni–Co, Ni–Mo, Cr–Cr, and Ni–Ni pairing in the FCC solid-solution have been noted in previous simulation studies [25,30]. These NN pairs are structural units necessary

to obtain the local ordering at the SFs and the short-range clusters outside the SFs (Fig. 5b-II and 5b-III). If the only Ni atom in the 1NNP of ALL#278 supercell is swapped with the Co atom in the 2NNP below the SF, the two 1NNPs constitute an entire D0₁₉-structured Co₃Mo unit cell, and the γ_{773} decreases from -528 to -794 mJ/m². However, the presence of entire Co₃Mo unit cell at SFs without any Ni substitution for Co was the result of manipulation; it was not formed in the MC simulation owing to the strong tendencies of the NN pairing between Ni and Co/Mo. This may lead to the lesser degrees of Co enrichment and Ni depletion at the SFs, which were the actual results from the STEM-EDS analysis (Fig. 1d and e). In contrast, Cr and Fe atoms were heavily depleted at the SFs. Swapping the Cr atom in the 2NNP below the SF of ALL#278 supercell with the Co and Ni atoms in the 1NNP was attempted, producing the ALL#278-Cr-Co-1, ALL#278-Cr-Co-2, and ALL#278-Cr-Ni supercells shown in Fig. 5b-IV, V, and VI, respectively. As seen in Fig. 5c, the altered supercells gain the large increases in the energy of full-relaxed supercell (E_R). Second, the segregation of the Cr atom also increases the γ_{773} of ALL#278-Cr-Co-1 and ALL#278-Cr-Co-2 supercells. In contrast, the γ_{773} of ALL#278-Cr-Ni supercell does not increase much. This indicates the synergistic role of Mo with Co rather than with Cr and Ni for the low γ_{773} . Because Cr and Mo in the same group have close chemical properties, the pre-existing Mo atoms at the SFs weaken the chemical segregation tendency of Cr atoms. Accordingly, the NN Mo-Cr pair is absent in the SF region of ALL#130 and ALL#278 supercells. It was reported by experimentalists that Cr atoms have strong tendencies to form nanoscale clusters [31] and Cr-rich, Ni-depleted σ and body-centered-cubic phases [32,33] in FCC alloys. Meanwhile, Cr and Fe have a strong attraction between them to form σ phases [34]. When Cr atoms are excluded from the Mo-enriched region at SFs, predominantly Cr and fewer Fe atoms form the short-range clusters outside SFs.

On the other hand, Cr is usually one of the Suzuki segregation elements in FCC alloys [9,11,35]. In Fig. 5b-II and 5b-III, the Cr atom in the 2NNP below the SF of supercells is the 2NN to the Mo atom in the 1NNP. As the Cr atom in the 2NNP can take part in the local D0₁₉-type ordering through the 2NN Mo-Cr interaction, the detected excess of Mo atoms at SFs was lower than expected from the exact concentration value of bulk D0₁₉ Co₃Mo (i.e., 25 at% Mo). The lesser degree of Cr depletion than Fe (Fig. 1e) can be also interpreted. After swapping the 2NN Cr atom (2NNP) with the Mo atom (1NNP) below the SF of ALL#278 supercell, the ALL#278-Cr-Mo supercell in Fig. 5b-VII is generated. In this process, the E_R increases marginally, while the γ_{773} increases considerably by 167 mJ/m² (Fig. 5c). This indicates that Cr in the SF region can replace a part of roles of Mo, despite the weakened segregation tendency and Suzuki effect. One feature of the studied HEA is that it contains high-concentration Mo atoms. One can also envisage that the present

simulation approach can be applied directly in a broad range of alloys. For example, if Mo concentration of alloys is insufficiently high [9,36], Cr atoms may segregate at SFs as well.

4.3. Stability of Co/Mo co-segregated SFs

Moreover, the FCC solid-solution alloy remained stable after 72h-aging at 773 K (Fig. 6). The D0₁₉-type ordering at SFs must complete compositional and structural transitions to form thermodynamically stable topologically close-packed (TCP) phases, namely, μ and σ phases that are frequent in FCC CoCrFeNiMo HEAs [37–39]. μ and σ phases are predominantly enriched in Mo and Cr. As stated, already segregated Mo atoms at the SFs would impede the further segregation of Mo and Cr atoms. Although the Mo segregation at SFs might lead one to suppose that it is favorable for the TCP phase precipitation, the compositional transition remains an obstacle towards the formation of intermetallics at SFs. Owing to co-segregation of Co and finite Mo atoms and the anti-segregation of Cr atoms, the SF is expected to have high dynamical stability. This analysis is helpful in the prediction of local phase transitions at SFs [40]. Furthermore, a negative local SFE does not denote the possibility of isothermal martensitic transformation. The global SFE of alloy is 53 mJ/m² at 773 K [41], indicating that the FCC structure is more stable than the HCP structure for the alloy. If the global SFE of alloy is as low as a negative value, the SF is on the verge of expansion and the martensitic transition easily occurs by massive Shockley partial dislocations slipping on every second {111} plane [42]. Thus, the Co_{0.95}Cr_{0.8}Fe_{0.25}Ni_{1.8}Mo_{0.475} solid-solution alloy with Co/Mo co-segregated SFs retains the thermodynamic stability against the phase transition to martensite when annealed at 773 K.

5. Conclusions

In this work, we used the two-stage first-principles MC simulations each with up to 3000 trial swap steps to decrypt the subtle physical phenomenon of Co/Mo co-segregation at SFs. The main conclusions are summarized as follows.

- (1) Relatively homogeneous distribution of Mo atoms in the solid-solution is beneficial for the overall small lattice distortion; conversely, clustering of Mo atoms induces an increase in local intrinsic strain and energy. Mo atoms exhibit the strong tendency of segregation at SFs. With the segregation of Mo atoms at SFs, the local intrinsic strain increases and may become too large. Apart from the chemical energy, the increase in intrinsic strain energy is an essential factor for finite Suzuki segregation of Mo in the

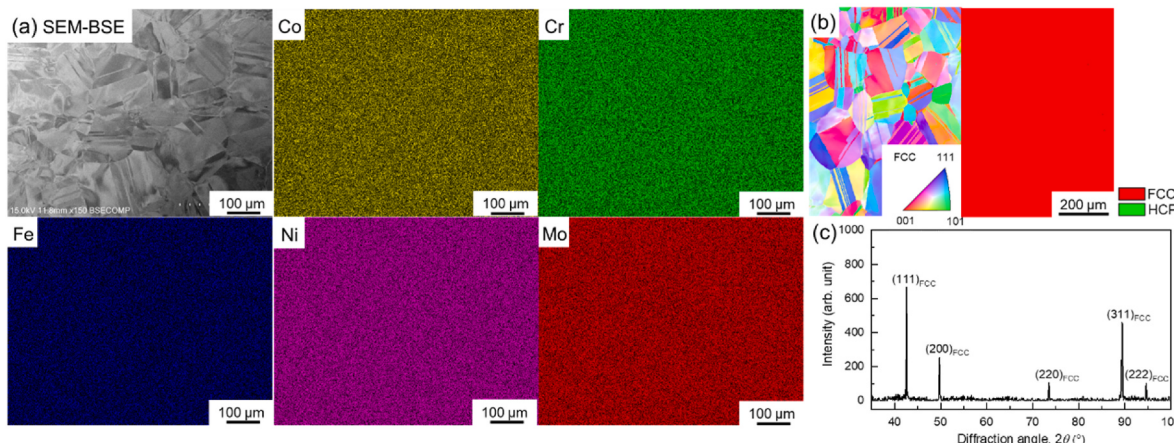


Fig. 6. (a) SEM-backscattered electron image and EDS elemental distribution maps for the tensile-strained specimen after 72h-aging at 773 K, which show the uniform compositional distribution. (b) EBSD inverse pole figure map and phase map (confidence index > 0.1), where only FCC phase can be identified. (c) XRD pattern of the specimen showing the peaks only for FCC phase.

- CoCrFeNi-based solid-solution alloys. It is thus suggested that there is saturation Mo concentration for Suzuki segregation in high-Mo-concentration alloys.
- (2) The first-principles MC simulations yield the local D₀₁₉-type ordering at SFs, primarily comprising Co and Mo atoms. Ni atoms substitute a small part of Co atoms in the local ordering, which leads to lower degrees of Co enrichment and Ni depletion at SFs. Moreover, Cr atoms are excluded from the Mo-enriched region at SFs; predominantly Cr and fewer Fe atoms form the short-range clusters outside SFs, which leads to the depletion of Cr and Fe at SFs. Additionally, the energetically stable supercells in the MC simulation imply that Cr atoms could substitute Mo atoms in the local D₀₁₉-type ordering, which leads to the lesser depletion of Cr than Fe. Cr is a potential element of segregation, when Mo is insufficient. The simulation result is consistent with the experimentally detected degree of elemental enrichment and depletion at SFs. Further, the simulations provide additional insights into the experimental phenomena.
- (3) The SF with the local D₀₁₉-type ordering of Co and Mo atoms produces a moderate lattice distortion and a strongly negative SFE. Nonetheless, the SF has high dynamical stability against the second-phase precipitation and high thermodynamic stability against martensitic transition at 773 K.
- (4) In the light of this study, it is expected that the co-segregation of Co and Mo atoms would also take place at other planar defects in Co_{0.95}Cr_{0.8}Fe_{0.25}Ni_{1.8}Mo_{0.475} HEAs like twin boundaries, which have the similar ABAB-type stacking HCP structure to SFs.

Funding

The work was supported by the Grant-in-Aid for Scientific Research [KAKENHI Grant No. 18H05455] from the Japan Society for the Promotion of Science; and the State-funded Postdoctoral Researcher Program [Grant No. GZC20232377] from the China Postdoctoral Science Foundation.

CRediT authorship contribution statement

Jiaxiang Li: Writing – original draft, Visualization, Validation, Methodology, Investigation, Formal analysis, Data curation, Conceptualization. **Kenta Yamanaka:** Writing – review & editing, Supervision, Project administration. **Junhua Hu:** Writing – review & editing. **Akihiko Chiba:** Supervision, Project administration, Funding acquisition.

Declaration of competing interest

The authors declare that they have no known competing financial interests or personal relationships that could have appeared to influence the work reported in this paper.

Data availability

Data will be made available on request.

Acknowledgement

The computations were carried out under the GIMRT program of the Center for Computational Materials Science, Institute for Materials Research, Tohoku University, Japan (Proposal No. 20S0406, 202012-SCKXX-0403, 202112-SCKXX-0406).

Appendix A. Supplementary data

Supplementary data to this article can be found online at <https://doi.org/10.1016/j.mtphys.2024.101468>.

References

- [1] H. Suzuki, Sci Rep Res Inst Tohoku Univ A 4 (1952) 455–463.
- [2] P.A. Flinn, Solute hardening of close-packed solid solutions, Acta Metall. 6 (1958) 631–635.
- [3] D. Sorenson, B.Q. Li, W.W. Gerberich, K.A. Mkhoyan, Investigation of secondary hardening in Co–35Ni–20Cr–10Mo alloy using analytical scanning transmission electron microscopy, Acta Mater. 63 (2014) 63–72.
- [4] K. Ming, X. Bi, J. Wang, Segregation of Mo atoms into stacking faults in CrFeCoNiMo alloy, Philos. Mag. A 99 (2019) 1014–1024.
- [5] D.B. Miracle, O.N. Senkov, A critical review of high entropy alloys and related concepts, Acta Mater. 122 (2017) 448–511.
- [6] E.J. Pickering, N.G. Jones, High-entropy alloys: a critical assessment of their founding principles and future prospects, Int. Mater. Rev. 61 (2016) 183–202.
- [7] B. Gludovatz, E.P. George, R.O. Ritchie, Processing, microstructure and mechanical properties of the CrMnFeCoNi high-entropy alloy, JOM 67 (2015) 2262–2270.
- [8] P. Sathiyamoorthi, P. Asghari-Rad, J.W. Bae, H.S. Kim, Fine tuning of tensile properties in CrCoNi medium entropy alloy through cold rolling and annealing, Intermetallics 113 (2019) 106578.
- [9] Y. Koizumi, T. Nukaya, S. Suzuki, S. Kurosu, Y. Li, H. Matsumoto, K. Sato, Y. Tanaka, A. Chiba, Suzuki segregation in Co–Ni-based superalloy at 973 K: an experimental and computational study by phase-field simulation, Acta Mater. 60 (2012) 2901–2915.
- [10] G.W. Han, I.P. Jones, R.E. Smallman, Direct evidence for Suzuki segregation and Cottrell pinning in MP159 superalloy obtained by FEG(S)TEM/EDX, Acta Mater. 51 (2003) 2731–2742.
- [11] L. Feng, Y. Rao, M. Ghazisaeidi, M.J. Mills, Y. Wang, Quantitative prediction of Suzuki segregation at stacking faults of the γ' phase in Ni-base superalloys, Acta Mater. 200 (2020) 223–235.
- [12] S. Curtze, V.T. Kuokkala, A. Oikari, J. Talonen, H. Hänninen, Thermodynamic modeling of the stacking fault energy of austenitic steels, Acta Mater. 59 (2011) 1068–1076.
- [13] T.L. Achmad, W. Fu, H. Chen, C. Zhang, Z.G. Yang, Effects of alloying elements concentrations and temperatures on the stacking fault energies of Co-based alloys by computational thermodynamic approach and first-principles calculations, J. Alloys Compd. 694 (2017) 1265–1279.
- [14] A. Chiba, X.G. Li, M.S. Kim, High work-hardening rate and deformation twinning of Co–Ni-based superalloy at elevated temperatures, Philos. Mag. A 79 (1999) 1533–1554.
- [15] Y.J. Xu, D.Q. Qi, K. Du, C.Y. Cui, H.Q. Ye, Stacking fault effects on dynamic strain aging in a Ni–Co-based superalloy, Scripta Mater. 87 (2014) 37–40.
- [16] G.W. Han, I.P. Jones, R.E. Smallman, Direct evidence for Suzuki segregation and Cottrell pinning in MP159 superalloy obtained by FEG(S)TEM/EDX, Acta Mater. 51 (2003) 2731–2742.
- [17] J.D. Poplawsky, B.K. Milligan, L.F. Allard, The synergistic role of Mn and Zr/Ti in producing δ'/L₁₂ co-precipitates in Al–Cu alloys, Acta Mater. 194 (2020) 577–586.
- [18] V.I. Razumovskiy, S.V. Divinski, L. Romaner, Solute segregation in Cu: DFT vs. Experiment, Acta Mater. 147 (2018) 122–132.
- [19] J. Li, K. Yamanaka, A. Chiba, Calculation-driven design of off-equatomic high-entropy alloys with enhanced solid-solution strengthening, Mater. Sci. Eng., A 817 (2021) 141359.
- [20] G. Kresse, J. Furthmüller, Efficiency of ab-initio total energy calculations for metals and semiconductors using a plane-wave basis set, Comput. Mater. Sci. 6 (1996) 15–50.
- [21] S. Zhao, G.M. Stocks, Y. Zhang, Stacking fault energies of face-centered cubic concentrated solid solution alloys, Acta Mater. 134 (2017) 334–345.
- [22] J.A. Zimmerman, H. Gao, F.F. Abraham, Generalized stacking fault energies for embedded atom FCC metals, Model. Simulat. Mater. Sci. Eng. 8 (2000) 103.
- [23] A. Togo, F. Oba, I. Tanaka, First-principles calculations of the ferroelastic transition between rutile-type and CaCl₂-type SiO₂ at high pressures, Phys. Rev. B 78 (2008): 134106.
- [24] M.S. Titus, R.K. Rhein, P.B. Wells, P.C. Dodge, G.B. Viswanathan, M.J. Mills, A. V. der Ven, T.M. Pollock, Solute segregation and deviation from bulk thermodynamics at nanoscale crystalline defects, Sci. Adv. 2 (2016): e1601796.
- [25] J. Li, K. Yamanaka, A. Chiba, Influence of interatomic interactions on the mechanical properties of face-centered cubic multicomponent Co–Ni–Cr–Mo alloys, Materialia 12 (2020): 100742.
- [26] S.K. Makineni, A. Samanta, T. Rojhirunsakool, T. Alam, B. Nithin, A.K. Singh, R. Banerjee, K. Chattopadhyay, A new class of high strength high temperature Cobalt based γ–γ' Co–Mo–Al alloys stabilized with Ta addition, Acta Mater. 97 (2015) 29–40.
- [27] L. Alte da Veiga, Refinement of the structure of the phase Co₃Mo, Acta Crystallogr. 18 (1965) 855–857.
- [28] Q. Ding, Y. Zhang, X. Chen, X. Fu, D. Chen, S. Chen, L. Gu, F. Wei, H. Bei, Y. Gao, M. Wen, J. Li, Z. Zhang, T. Zhu, R.O. Ritchie, Q. Yu, Tuning element distribution, structure and properties by composition in high-entropy alloys, Nature 574 (2019) 223–227.
- [29] D. Wen, M.S. Titus, First-principles study of Suzuki segregation at stacking faults in disordered face-centered cubic Co–Ni alloys, Acta Mater. 221 (2021) 117358.
- [30] J. Ding, Q. Yu, M. Asta, R.O. Ritchie, Tunable stacking fault energies by tailoring local chemical order in CrCoNi medium-entropy alloys, Proc. Natl. Acad. Sci. USA 115 (2018) 8919–8924.
- [31] H. Shima, M. Mori, K. Yamanaka, K. Yoshida, T. Yamazaki, A. Chiba, Superior hardness-corrosion-resistance combination in a Co-, Cu-modified Ni–Cr–Mo alloy via multiple nanoscale segregation mechanisms, Scripta Mater. 209 (2022): 114389.

- [32] G. Laplanche, S. Berglund, C. Reinhart, A. Kostka, F. Fox, E.P. George, Phase stability and kinetics of σ -phase precipitation in CrMnFeCoNi high-entropy alloys, *Acta Mater.* 161 (2018) 338–351.
- [33] F. Otto, A. Dlouhý, A.K.G. Pradeep, M. Kubénová, D. Raabe, G. Eggeler, E. P. George, Decomposition of the single-phase high-entropy alloy CrMnFeCoNi after prolonged anneals at intermediate temperatures, *Acta Mater.* 112 (2016) 40–52.
- [34] W. Xiong, M. Selleby, Q. Chen, J. Odqvist, Y. Du, Phase equilibria and thermodynamic properties in the Fe-Cr system, *Crit. Rev. Solid State Mater. Sci.* 35 (2010) 125–152.
- [35] T.L. Achmad, W. Fu, H. Chen, C. Zhang, Z.G. Yang, Effect of solute segregation on the intrinsic stacking fault energy of Co-based binary alloys: a first-principles study, *J. Alloys Compd.* 748 (2018) 328–337.
- [36] H. Bian, X. Xu, Y. Li, Y. Koizumi, Z. Wang, M. Chen, K. Yamanaka, A. Chiba, Regulating the coarsening of the γ' phase in superalloys, *NPG Asia Mater.* 7 (2015): e212.
- [37] W.H. Liu, Z.P. Lu, J.Y. He, J.H. Luan, Z.J. Wang, B. Liu, Yong Liu, M.W. Chen, C. T. Liu, Ductile CoCrFeNiMo_x high entropy alloys strengthened by hard intermetallic phases, *Acta Mater.* 116 (2016) 332–342.
- [38] K. Ming, X. Bi, J. Wang, Precipitation strengthening of ductile Cr₁₅Fe₂₀Co₃₅Ni₂₀Mo₁₀ alloys, *Scripta Mater.* 137 (2017) 88–93.
- [39] H. Kwon, P. Asghari-Rad, J.M. Park, P. Sathiyamoorthi, J.W. Bae, J. Moon, A. Zargaran, Y.T. Choi, S. Son, H.S. Kim, Synergistic strengthening from grain refinement and nano-scale precipitates in non-equiautomatic CoCrFeNiMo medium-entropy alloy, *Intermetallics* 135 (2021): 107212.
- [40] T.M. Smith, B.S. Good, T.P. Gabb, B.D. Esser, A.J. Egan, L.J. Evans, D.W. McComb, M.J. Mills, Effect of stacking fault segregation and local phase transformations on creep strength in Ni-base superalloys, *Acta Mater.* 172 (2019) 55–65.
- [41] J. Li, K. Yamanaka, Y. Hayasaka, A. Chiba, Suzuki hardening and segregation in Co_{0.95}Cr_{0.8}Fe_{0.25}Ni_{1.8}Mo_{0.475} high-entropy alloys, *Scripta Mater.* 226 (2023): 115260.
- [42] Y. Koizumi, S. Suzuki, K. Yamanaka, B.S. Lee, K. Sato, Y. Li, S. Kurosu, H. Matsumoto, A. Chiba, Strain-induced martensitic transformation near twin boundaries in a biomedical Co-Cr-Mo alloy with negative stacking fault energy, *Acta Mater.* 61 (2013) 1648–1661.